Stellar Populations of Lyman Break Galaxies at $z \simeq 1$–3 in the HST/WFC3 Early Release Science Observations

N. P. Hathi[1], S. H. Cohen[2], R. E. Ryan Jr.[3], S. L. Finkelstein[4], P. J. McCarthy[1], R. A. Windhorst[2], H. Yan[5], A. M. Koekemoer[3], M. J. Rutkowski[2], R. W. O'Connell[6], A. N. Straughn[7], B. Balick[8], H. E. Bond[3], D. Calzetti[9], M. J. Disney[10], M. A. Dopita[11,12], Jay A. Frogel[12,13], D. N. B. Hall[14], J. A. Holtzman[15], R. A. Kimble[7], F. Paresce[16], A. Saha[17], J. I. Silk[18], J. T. Trauger[19], A. R. Walker[20], B. C. Whitmore[3], and E. T. Young[21]

nhathi@obs.carnegiescience.edu

ABSTRACT

[1]Observatories of the Carnegie Institution for Science, Pasadena, CA 91101, USA

[2]School of Earth and Space Exploration, Arizona State University, Tempe, AZ 85287-1404, USA

[3]Space Telescope Science Institute, Baltimore, MD 21218, USA

[4]Department of Astronomy, The University of Texas, Austin, TX 78712, USA

[5]Department of Physics & Astronomy, University of Missouri, Columbia, MO 65211, USA

[6]Department of Astronomy, University of Virginia, Charlottesville, VA 22904-4325, USA

[7]NASA–Goddard Space Flight Center, Greenbelt, MD 20771, USA

[8]Department of Astronomy, University of Washington, Seattle, WA 98195-1580, USA

[9]Department of Astronomy, University of Massachusetts, Amherst, MA 01003, USA

[10]School of Physics and Astronomy, Cardiff University, Cardiff CF24 3AA, UK

[11]Research School of Astronomy & Astrophysics, The Australian National University, ACT 2611, Australia

[12]Astronomy Department, King Abdulaziz University, P.O. Box 80203, Jeddah, Saudi Arabia

[13]Galaxies Unlimited, 1 Tremblant Court, Lutherville, MD 21093, USA

[14]Institute for Astronomy, University of Hawaii, Honolulu, HI 96822, USA

[15]Department of Astronomy, New Mexico State University, Las Cruces, NM 88003, USA

[16]Istituto di Astrofisica Spaziale e Fisica Cosmica, INAF, Via Gobetti 101, 40129 Bologna, Italy

[17]National Optical Astronomy Observatories, Tucson, AZ 85726-6732, USA

[18]Department of Physics, University of Oxford, Oxford OX1 3PU, UK

[19]NASA–Jet Propulsion Laboratory, Pasadena, CA 91109, USA

[20]Cerro Tololo Inter-American Observatory, La Serena, Chile

[21]NASA–Ames Research Center, Moffett Field, CA 94035, USA

We analyze the spectral energy distributions (SEDs) of Lyman break galaxies (LBGs) at $z \simeq 1$–3 selected using the *Hubble Space Telescope* (*HST*) Wide Field Camera 3 (WFC3) UVIS channel filters. These *HST*/WFC3 observations cover about 50 arcmin^2 in the GOODS-South field as a part of the WFC3 Early Release Science program. These LBGs at $z \simeq 1$–3 are selected using dropout selection criteria similar to high redshift LBGs. The deep multi-band photometry in this field is used to identify best-fit SED models, from which we infer the following results: (1) the photometric redshift estimate of these dropout selected LBGs is accurate to within few percent; (2) the UV spectral slope β is redder than at high redshift ($z > 3$), where LBGs are less dusty; (3) on average, LBGs at $z \simeq 1$–3 are massive, dustier and more highly star-forming, compared to LBGs at higher redshifts with similar luminosities, though their median values are similar within 1σ uncertainties. This could imply that identical dropout selection technique, at all redshifts, find physically similar galaxies; and (4) the stellar masses of these LBGs are directly proportional to their UV luminosities with a logarithmic slope of $\sim$0.46, and star-formation rates are proportional to their stellar masses with a logarithmic slope of $\sim$0.90. These relations hold true — within luminosities probed in this study — for LBGs from $z \simeq 1.5$ to 5. The star-forming galaxies selected using other color-based techniques show similar correlations at $z \simeq 2$, but to avoid any selection biases, and for direct comparison with LBGs at $z > 3$, a true Lyman break selection at $z \simeq 2$ is essential. The future *HST* UV surveys, both wider and deeper, covering a large luminosity range are important to better understand LBG properties, and their evolution.

Subject headings: galaxies: high redshift — galaxies: fundamental parameters — ultraviolet: galaxies — galaxies: evolution

1. Introduction

The high redshift frontier has moved to $z > 7$ as a result of the high resolution near-infrared (NIR) images from the *Hubble Space Telescope* (*HST*) Wide Field Camera 3 (WFC3), and the Lyman break 'dropout' technique. The Lyman break technique was first applied to select Lyman break galaxies (LBGs) at $z \simeq 3$ (Guhathakurta et al. 1990; Steidel et al. 1996, 1999), and since then it has been extensively used to select and study LBG candidates at redshifts $z \simeq 3$–8 (e.g., Bouwens et al. 2007; Hathi et al. 2008b; Reddy & Steidel 2009; Finkelstein et al. 2010; Yan et al. 2010). This dropout technique has generated large samples of faint star-forming galaxy candidates at $z \simeq 3$–8. However, at highest redshifts

($z > 3$), it is very difficult to understand the details of their stellar populations using current space and ground-based telescopes. Their faint magnitudes make it extremely difficult to do spectroscopic studies, and limited high resolution rest-frame optical photometry make it challenging to investigate their spectral energy distributions (SEDs). These limitations make it imperative to identify and study LBGs at lower redshifts ($z \lesssim 3$). The primary reason for the lack of dropout selected LBGs at $z \simeq 1$–3 is that we need highly sensitive space-based cameras to observe the mid- to near-ultraviolet (UV) wavelengths required to identify Lyman break at $z \simeq 1$–3. The peak epoch of global star-formation rate at $z \simeq 1$–3 is now accessible using the dropout technique with the WFC3 UVIS channel. Hathi et al. (2010, hereafter H10) and Oesch et al. (2010) have used the *HST* WFC3 with its superior sensitivity to photometrically identify lower redshift ($z \simeq 1$–3) LBGs. Understanding the LBGs at $z \lesssim 3$ is vital for two main reasons. First, we need to study the star-formation properties of these LBGs, because they are at redshifts corresponding to the peak epoch of the global star-formation rate (e.g., Ly et al. 2009; Bouwens et al. 2010). Second, they are likely lower redshift counterparts of the high redshift LBGs — because of their identical dropout selection and similar physical properties — whose understanding will help shed light on the process of reionization in the early universe (e.g., Labbé et al. 2010; Stark et al. 2010).

There are primarily three techniques to select star-forming galaxies at $z \simeq 2$: (1) *sBzK* (using the B, z, K bands, Daddi et al. 2004, 2007), (2) BX/BM (using the U, G, R bands, Steidel et al. 2004; Adelberger et al. 2004), and (3) LBG (using the bands which bracket the redshifted Lyman limit, H10; Oesch et al. 2010). All these approaches select star-forming galaxies, and yield insight into the star-forming properties of these galaxies, but they have differing selection biases, and so these samples don't completely overlap (see Ly et al. 2011; Haberzettl et al. 2012, for details). Therefore, it is essential to apply identical selection criteria at all redshifts to properly compare galaxy samples and accurately trace their evolution. The LBG selection is widely used to select high redshift ($z > 3$) galaxies, and to do equal comparison with these galaxies, here we investigate physical properties of LBGs at $z \lesssim 3$.

H10 used UV observations of the WFC3 Science Oversight Committee Early Release Science extragalactic program (PID: 11359, PI: O'Connell; hereafter "ERS"), which covers approximately 50 arcmin^2 in the northern-most part of the Great Observatories Origins Deep Survey (GOODS; Giavalisco et al. 2004) South field, to identify LBGs at $z \simeq 1$–3. The high sensitivity of the WFC3 UVIS channel data (Windhorst et al. 2011), along with existing deep optical data obtained with the Advanced Camera for Surveys (ACS) as part of the GOODS program are ideal to apply dropout technique in observed UV filters to select LBG candidates at $z \simeq 1$–3. In this paper, we use this H10 sample of LBGs to investigate their physical properties by fitting stellar synthesis models to their observed SEDs.

This paper is organized as follows: In § 2, we summarize the WFC3 ERS observations, and discuss our LBG sample at $z \simeq 1$–3 as well as the comparison sample of LBGs at $z \simeq 4$–5. In § 3, we fit observed SEDs of LBGs at $z \simeq 1$–3 and $z \simeq 4$–5 to stellar population synthesis models, and discuss the best-fit parameters (redshift, UV spectral slope, stellar mass, stellar age, and star-formation rates) obtained from these SED fits. In § 4, we discuss correlations between best-fit physical parameters and their implications on our understanding of LBGs. In § 5, we conclude with a summary of our results.

In the remaining sections of this paper we refer to the *HST*/WFC3 F225W, F275W, F336W, F098M, F125W, F160W, filters as U_{225}, U_{275}, U_{336}, Y_{098}, J_{125}, H_{160}, to the *HST*/ACS F435W, F606W, F775W, F850LP filters as B_{435}, V_{606}, i_{775}, z_{850}, and to the *Spitzer*/IRAC 3.6 μm, 4.5 μm filters as [3.6], [4.5], respectively, for convenience. We assume a *Wilkinson Microwave Anisotropy Probe* (WMAP) cosmology with Ω_m=0.274, Ω_Λ=0.726 and H_0=70.5 km s^{-1} Mpc^{-1}, in accord with the 5 year WMAP estimates of Komatsu et al. (2009). This corresponds to a look-back time of 10.4 Gyr at $z \simeq 2$. Magnitudes are given in the AB$_\nu$ system (Oke & Gunn 1983).

2. Observations and Sample Selection

The WFC3 ERS observations (Windhorst et al. 2011) were done in both the UVIS (with a FOV of 7.30 arcmin^2) and the IR (with a FOV of 4.65 arcmin^2) channels. Here, we briefly summarize the UV imaging observations. The WFC3 ERS UV observations were carried out in three broad-band filters U_{225}, U_{275} and U_{336}. The U_{225} and U_{275} filters were observed for 2 orbits (~5688s) per pointing, while the U_{336} filter was observed for 1 orbit (~2778 s) per pointing, for a total of 40 orbits over the full ERS field (8 pointings). We used the existing GOODS v2.0[1] reduction of the ACS images in four optical bands (B_{435}, V_{606}, i_{775}, z_{850}), which were re-binned to a pixel size of 0.09″. To match the ERS IR (Y_{098}, J_{125}, H_{160}) and re-pixellated ACS optical images, the UV mosaics have a pixel scale of 0.090″ pix^{-1} and cover ~50 arcmin^2 area of the GOODS-South field. Details of these observations and reduction process are described in Windhorst et al. (2011).

The combination of the three WFC3 UV filters and the four ACS optical filters provide an excellent ability to select LBGs at $z \simeq 1$–3 (H10; Oesch et al. 2010), using the dropout technique to detect the Lyman-break at rest-frame 912 Å (Madau 1995). H10 used dropout color selection technique in the ERS UV field to identify three sets of UV-dropouts — U_{225}-dropouts, U_{275}-dropouts and U_{336}-dropouts — which are LBG candidates at $z \simeq 1.6$, 2.2 and

[1]http://archive.stsci.edu/pub/hlsp/goods/v2/

2.6, respectively. They found 66 U_{225}-, 151 U_{275}- and 256 U_{336}-dropouts to a magnitude limit of AB $\simeq$ 26.5 mag, respectively.

In this paper, we start with the H10 LBG sample. Our goal is to investigate SEDs of reliable LBG candidates with at least 10-band HST coverage (augmented by additional data as described in § 3) from the H10 sample, so we apply the following filtering criteria. First criterion is the availability of the WFC3 IR (Y_{098}, J_{125}, H_{160}) data. H10 used the WFC3 UVIS and ACS data to select LBGs at $z \simeq$ 1–3. The WFC3 UVIS channel has a larger final ERS mosaic than the WFC3 IR channel, so we exclude LBG candidates that don't have WFC3 IR data from our SED analysis. This criterion reduces the H10 sample size by about 10%. Secondly, galaxies with poor SED fits (see § 3) as measured by their larger χ^2 were excluded from the sample. This criterion removes additional ~10% of galaxies from the H10 sample. This fraction of catastrophic χ^2 outliers is consistent with the outlier fraction in the photometric redshift distribution of the dropouts in the H10 sample. The final sample of LBGs for the SED analysis — after applying above mentioned criteria — is 47 U_{225}-, 126 U_{275}- and 213 U_{336}-dropouts.

To compare SED properties of LBGs at $z \simeq$ 1–3, we select B_{435}- and V_{606}-dropouts in the WFC3 ERS field. These dropouts — LBG candidates at $z \simeq$ 3.7 and 4.7, respectively — were selected following the Bouwens et al. (2007) selection criteria. The H10 sample is a comparatively brighter ($\sim M^*_{\rm uv}$) sample, because of the limited depth and area of the ERS data, and hence, we also limit our comparison B_{435}- and V_{606}-dropout sample to be around $\sim M^*_{\rm uv}$. Applying similar filtering criteria as LBGs at $z \simeq$ 1–3, we have a comparison sample of 155 B_{435}-dropouts and 27 V_{606}-dropouts in the ERS field. Based on Xue et al. (2011) X-ray catalog, there are four active galactic nuclei (AGN) in the H10 LBG sample ($z \lesssim 3$), three AGN in the B_{435}-dropout sample, and none in the V_{606}-dropout sample. These small number of X-ray AGN does not affect our results or conclusions.

All subsequent analysis in this paper is done identically on these 5 samples (U_{225}-, U_{275}-, U_{336}-, B_{435}-, and V_{606}-dropouts) for proper comparison. To show general evolutionary trends, we combine three dropout samples from H10 as a UV-dropout sample ($z \simeq$ 1–3), and two high redshift samples as a B_{435}-,V_{606}-dropout sample ($z \simeq$ 4–5).

3. Spectral Energy Distributions

The Le PHARE software package (Arnouts et al. 1999; Ilbert et al. 2006) was used to measure the photometric redshifts, and to fit the broadband SEDs of LBGs. The primary goal of SED fitting is to find the best-fitting synthetic stellar population model to the observed

photometry. From this best-fit model, we can estimate the redshift, stellar age, stellar mass, star-formation rate (SFR), dust extinction, and other physical properties of each galaxy. We use the 2007 version of the Bruzual & Charlot (2003, hereafter CB07) models, which has improved prescription of thermally pulsating AGB stars. We generated a set of stellar population models assuming a Salpeter initial mass function, and varying the redshift (z = 0.1–6.0, δz=0.1), metallicity (0.2, 0.4 and 1 $Z_{\odot}$), age (1 Myr $\leq t \leq t_H$), dust extinction (0 $\leq$ E(B-V) $\leq$ 0.7 mag, using a modified Calzetti et al. 2000 attenuation law), and e-folding timescale (τ=0.1–30 Gyr) for a star-formation history (SFH) $\propto$ exp(-t/τ). The Le PHARE code assumes the Madau (1995) prescription to estimate inter-galactic medium (IGM) opacity. The model that gives the lowest χ^2 is chosen as the best-fit SED.

The contribution of major emission lines in different filters can be included in the models using the Le PHARE code. Neglecting emission lines during the SED fitting process can overestimate the best-fit stellar ages and masses by about 0.3 dex (e.g., Schaerer & de Barros 2009; Finkelstein et al. 2011; Atek et al. 2011). The Le PHARE code accounts for the contribution of emission lines with a simple recipe based on the Kennicutt (1998) relations between the SFR and UV luminosity, Hα and [OII] lines. The code includes the Lyα, Hα, Hβ, [OII], OIII[4959] and OIII[5007] lines with different line ratios with respect to [OII] line, as described in Ilbert et al. (2009).

The observed photometry is available in up to 13 filters: three *HST*/WFC3 UVIS, four *HST*/ACS, three *HST*/WFC3 IR, one VLT Ks, and two *Spitzer*/IRAC [3.6], [4.5] bands. We perform matched aperture photometry in 10 *HST* bands as discussed in H10, while we use VLT and *Spitzer* photometry from the publicly available GOODS-MUSIC catalog (Santini et al. 2009). The photometry in MUSIC catalog has accurate PSF-matching of space and ground-based images of different resolution and depth. Figure 1 shows example best-fit SEDs for LBGs at $z \simeq$ 1–3, and the comparison sample of LBGs at $z \simeq$ 4–5.

3.1. Photometric Redshifts

One of the free parameters during the SED fitting process is the redshift. To assess the accuracy of our SED-based photometric redshifts (z_{ph}) at $z \simeq$ 1–3, we compare them with the spectroscopic redshifts (z_{sp}) from various VLT/Magellan campaigns in the GOODS-S field (e.g., Grazian et al. 2006; Ravikumar et al. 2007; Vanzella et al. 2008; Wuyts et al. 2008; Balestra et al. 2010; Cooper et al. 2011). We find that only a small number ($\lesssim$30%) of our total dropout sample (H10) has spectroscopic redshifts, most likely due to the lack of strong features in 4500–9000 Å range at $1 \lesssim z \lesssim 3$, where most ground-based spectrographs on large telescopes are optimized. We matched 91 spectroscopic redshifts for the UV-dropout

sample ($z \simeq 1$–3) selected with the criteria discussed in § 2. Figure 2 shows the comparison between the SED based photometric redshifts and the publicly available spectroscopic redshifts. The catastrophic outliers — shown by concentric circles in Figure 2 — have quality flags that indicate the spectroscopic redshift is unreliable (in most catalogs C or worst). So it is likely that these spectroscopic redshifts are not correct and hence, redshift comparison for these objects is not credible. The histogram in Figure 2 shows the distribution of photometric redshift uncertainties δz=($z_{sp} - z_{ph}$/1+z_{sp}). Based on this distribution, we estimate $\sigma(\delta z)\simeq$0.05, and $< \delta z >$=–0.03. The fraction of catastrophic outliers (>3σ) is ~7%, excluding objects with unreliable spectroscopic redshifts. Our photometric redshift uncertainties are consistent with Dahlen et al. (2010), who used the deepest and the most comprehensive photometric data in the GOODS-S field. Haberzettl et al. (2012) selected fairly bright LBGs at $z \simeq 2$ using the *GALEX* data, and found similar photometric redshift uncertainties and outlier fraction for their dropout sample. The photometric redshift uncertainty in the implied redshift is also consistent with the dropout selection method applied to select these galaxies. The dropout selection technique uses the location of a spectral break within a photometric bandpass (filter), and therefore, the redshift uncertainty depends on the width of the bandpass, and could be as high as ~0.5 in z.

The distribution of photometric redshift uncertainties (δz) is asymmetric, even after excluding objects with unreliable spectroscopic redshifts. There are more galaxies in the distribution with spectroscopic redshifts lower than their photometric redshifts i.e., ($z_{sp} - z_{ph} < 0$). Detail investigation of each ground-based spectra (if available) is needed to figure out what is causing spectroscopic redshift to be lower than photometric redshift. Such an investigation is beyond the scope of this paper, but we should point out that such asymmetric distribution is also observed for *GALEX*–selected LBGs (e.g., Haberzettl et al. 2012), and is totally consistent within the estimated photometric redshift uncertainties.

3.2. UV Spectral Slope β

The UV spectral slope β is determined from a power-law fit to the UV continuum spectrum (Calzetti et al. 1994), $f_\lambda \propto \lambda^\beta$, where f_λ is the flux density per unit wavelength (ergs s^{-1} cm^{-2} Å^{-1}). We use the best-fit SEDs of dropout selected LBGs to estimate their UV spectral slope β by fitting a straight line between rest-frame 1300 and 1900 Å in their model spectrum. This wavelength range covers 7 out of 10 spectral fitting windows identified by Calzetti et al. (1994) to estimate the UV spectral slope. This wavelength range is also ideal for comparing β values at higher redshifts, because those are usually measured between rest-frame 1600 and 2000 Å. Figure 3 shows the slope-fitting method applied to the best-fit

SEDs to estimate β, where the solid line is the best-fit UV spectral slope, the dashed line is the best-fit SED, and the black filled circles are observed magnitudes. By selection (§ 2), we only consider galaxies with good SED fits so the choice of model should not affect the β estimate. We estimate β for each galaxy, and then fit a Gaussian to the β distribution to find median (and sigma) value in each redshift bin. Table 1 shows median β values and their corresponding uncertainties for the UV-dropout, and the B_{435}-,V_{606}-dropout samples.

The evolution in the UV spectral slope β as a function of redshift may indicate change in stellar populations of galaxies over cosmic time. We compare our β values with the higher redshift measurements from the literature (e.g., Bouwens et al. 2011; Finkelstein et al. 2012). Figure 4 shows the UV spectral slope β as a function of redshift. Blue filled squares are median β values measured between rest-frame 1300 and 1900 Å for our dropout samples. To test how β measurements are affected by the selection of rest-frame UV wavelength range, we also measured β between rest-frame 1300 and 3400 Å, which are shown by blue open squares in Figure 4. Both β values agree within 1σ uncertainties. The red filled diamonds are measurements from Bouwens et al. (2009, 2011) and purple filled circles are from Finkelstein et al. (2012). The β values from Bouwens et al. (2009, 2011) are for the galaxies around $M^*_{\rm uv}$, which is consistent with our sample, while Finkelstein et al. (2012) measurements are based on all galaxies extending to those fainter than $M^*_{\rm uv}$ in their respective redshift bins. The uncertainties on the median values of β are the standard error of the mean in the case of Finkelstein et al. (2012) and our measurements, while Bouwens et al. (2009, 2011) uncertainties represent 1σ scatter. For comparison, our estimated 1σ scatter in median β values are listed in Table 1.

Figure 4 shows that the median values of β decreases as redshift increases ($\beta \simeq -1.6$ at $z \simeq 1.6$ to $\beta \simeq -2.4$ at $z \simeq 8$), which could imply variations in one or more physical properties of LBGs as a function of redshift. Figure 5 shows evolution in β as a function of best-fit SED parameters (stellar mass, stellar age, dust content, SFR) and redshift. The lowest redshift bin ($z \simeq 1.6$) is shown by the smallest circles, and the highest redshift bin ($z \simeq 4$–5) is shown by the largest circles. The largest change (factor of $\sim$2 or 0.3 dex) is seen in the dust content E(B–V) of galaxies as β changes from –1.6 (at $z \simeq 1.6$) to –1.9 (at $z \simeq 4$–5), while other three parameters vary much less than a factor of 2. This could imply that change in the dust content of LBGs has largest effect on the UV spectral slope β, and any variation in β as a function of redshift could most likely be due to changing dust content of galaxies. Therefore, based on our β estimates, as shown in Figure 4, we could say that LBGs at lower redshift ($z \simeq 1.6$) have more dust than LBGs at higher redshift ($z \simeq 5$). This trend of β is consistent with those from previous studies, which have found that galaxies at $z \simeq 6$ tend to be bluer than those at $z \simeq 3$ (e.g., Stanway et al. 2005; Bouwens et al. 2006; Hathi et al. 2008a; Wilkins et al. 2011). Those β measurements, on uniformly selected LBGs,

were limited to LBGs at $z \gtrsim 3$, and our results below $z \simeq 3$ extends this observed trend to $z \simeq 1.5$.

The evolution in the UV spectral slope β could also be due to changing star-formation history, initial mass function (IMF), and/or metallicity. These effects are believed to be much smaller than the effects from changing dust content of the galaxy. Many authors have investigated various stellar population models to estimate these effects. Bouwens et al. (2011) explored sensitivity of the UV-continuum slope β to changes in the mean metallicity, age, or dust extinction by choosing one fiducial model as a benchmark, and then changing various model parameters to assess changes in β. They conclude that a factor of 2 (or 0.3 dex) changes in metallicity, age or dust content result in 0.07, 0.15, 0.35 changes in the UV spectral slope β, respectively. This implies that changes in the dust content have much larger effect on the UV-continuum slope than similarly-sized changes in the age, metallicity, or the stellar IMF. Similar studies (e.g., Leitherer et al. 1999; Hathi et al. 2008a; Wilkins et al. 2011) have come to the same conclusion that though β could be affected by various stellar population properties, the change in dust content of galaxies is the predominant effect which causes β to change. We should also emphasize that it is very challenging to completely understand these various effects based on observations only, rigorous modeling and/or simulations are required to fully assess the contributions of these various effects on the UV spectral slope β.

3.3. Stellar Population Properties

We use the 10-band *HST* photometry along with the VLT Ks and the *Spitzer*/IRAC [3.6], [4.5] bands to construct an observed SED which we then compare to a suite of model templates from CB07 and find the best-fit model through χ^2 minimization. The model parameters are outlined in § 3. The best-fit model allows us to estimate stellar age, stellar mass, dust extinction E(B–V) and SFRs for each galaxy. Uncertainties (~0.3–0.4 dex) in stellar ages, masses and SFRs are estimated based on the uncertainties in redshift and observed photometry.

One of the main limitations of SED fitting is the need to assume a SFH, which cannot be reliably constrained for a galaxy from limited photometric data points. We have assumed an exponentially declining SFH. Different SFHs (e.g., rising, constant, declining) introduce systematic uncertainties in the stellar mass determinations, mostly at redshift greater than $z \simeq 3$ (e.g., Lee et al. 2010; Papovich et al. 2011). These uncertainties are typically $\lesssim$0.3 dex (e.g., Finlator et al. 2007), and are within our estimated uncertainties. Stellar ages are highly sensitive to the assumed SFH. Any prior star-forming episode can be overshadowed by newly born stars from the most recent star-formation, totally neglecting possible existence

of older population in a given galaxy. Therefore, based on assumed histories, it is possible to get an older or a younger age for the same galaxy. Hence, interpreting the stellar ages derived from SED fitting can be tricky, and at the very least, the uncertainties on the stellar ages could be much larger than estimated uncertainties (~0.3–0.4 dex). Because of these issues, in subsequent analysis, we will not elaborate on stellar population ages and focus on other physical properties.

Figure 6 shows the distributions of stellar age, stellar mass, SFRs, and E(B–V) for LBGs at $z \simeq$ 1–3 (black), and the comparison sample of LBGs at $z \simeq$ 4–5 (red). The median values are shown by dashed vertical lines and 1σ uncertainties in these distributions for LBGs at $z \simeq$ 1–3 are shown by an error bar at the top of the black histogram. A two-sided K-S test indicates a probability *less* than 0.006 that the distributions (red and black histograms) are drawn from the *same* parent distribution. Figure 6 shows a general trend that — on average — higher redshift LBGs have low SFRs, less dust, and are less massive than their lower redshift counterparts, though median values of two distributions (red and black) are similar within 1σ uncertainties. This result is in good agreement with previous studies comparing LBGs at $z \simeq 3$ and $z \simeq 5$ (e.g., Verma et al. 2007). The average E(B–V) at $z \simeq 2$ is consistent with studies based on star-forming galaxies selected using BX/BM color technique (e.g., Erb et al. 2006; Sawicki 2012). The distribution of E(B–V) completely agrees with the UV spectral slope evolution as discussed in § 3.2, implying that the LBGs at $z \simeq$ 1–3 are more dusty (redder) compared to LBGs at $z \simeq$ 4–5.

4. Results and Discussion

4.1. Stellar Mass vs UV Luminosity Relation

The rest-frame UV light traces current or instantaneous SFR, while rest-frame optical and NIR data help us to estimate stellar masses of galaxies. If the galaxy stellar mass and UV luminosity are related then we can directly use rest-frame UV light to estimate stellar mass without needing rest-frame optical/NIR data. Figure 7 shows stellar mass of LBGs at $z \simeq$ 1.5–5 as a function of their UV absolute magnitude. These quantities are based on best-fit SEDs, and their typical uncertainties are shown in the lower-left corner. The dotted lines are best-fit line obtained by keeping the logarithmic slope fixed at 0.46, which was estimated by Sawicki (2012) for star-forming galaxies at $z \simeq 2$. The dot-dash lines show the scatter from the best-fit line, which is ~0.3 dex for LBGs at $z \simeq$ 1–3 and about 0.2 dex for LBGs at $z \simeq$ 4–5. We also tested the validity of this relation by fitting the slope of the line rather than fixing it. We find that the fitted slope is in the range of 0.42±0.06 for our LBG samples, which is consistent with 0.46 within the estimated 1σ scatter in this relation. Therefore, we

find that a proportionality relation between these two parameters with a logarithmic slope of 0.46 provides a good fit to the data. The stellar masses of the brighter LBGs — with UV luminosities near the $L^*_{\rm uv}$ value of LBGs at $z \simeq 3$ from Steidel et al. (1999) — are about a factor of 2 lower than 10^{10} $M_\odot$ estimated by Papovich et al. (2001). This discrepancy, though within our estimated uncertainties, could be due to the fact that we include emission lines in our SED fitting which can affect stellar masses by a factor of ~2. The stellar mass–UV luminosity relation is fairly tight with a small scatter ($\lesssim$0.3 dex), which is consistent with other studies at similar redshifts (e.g., Papovich et al. 2001), and it points to a nearly constant mass-to-light ratio (log(M/L) $\simeq$ –0.5, see § 4.3) for LBGs between $z \simeq 1.5$ and 5. A similar correlation between stellar mass and absolute magnitude has been reported for LBGs at $z \simeq$ 5–6 by Stark et al. (2009).

Figure 7 shows that LBGs at $z \simeq$ 1.5–5 follow similar linear correlation between stellar mass and UV absolute magnitude (within uncertainties) for $M_{\rm uv}$ between –19 and –22.5 mag. It is important to note that Shapley et al. (2005) does not find any correlation between the stellar mass and UV absolute magnitude for star-forming galaxies at $z \simeq 2$ with stellar masses $\gtrsim 10^{10}$ $M_\odot$. This could be due to different color-selection technique (BX/BM) used by the Shapley et al. (2005) to select star-forming galaxies, whose physical properties could differ from the dropout selected LBGs at these masses (e.g., Ly et al. 2011; Haberzettl et al. 2012). It is also possible that their sample, which consists of spectroscopically confirmed bright galaxies with stellar masses greater than or equal to 10^{10} $M_\odot$, has more massive galaxies than our sample because of the limited survey area in the WFC3 ERS field. The ERS observations are too limited in area and depth to cover a larger luminosity range, so we cannot predict how this relation will evolve for luminous ($M_{\rm uv} < -22.5$ mag) or dwarf ($M_{\rm uv} > -19$ mag) galaxies at these redshifts.

4.2. SFR vs Stellar Mass

The correlation between the current SFR and stellar mass in star-forming galaxies, also known as 'main sequence of star-formation' (MS), has been observed at $z \lesssim 2$ (e.g., Noeske et al. 2007; Elbaz et al. 2007; Daddi et al. 2007). These studies have shown that the MS relation seems to be not evolving strongly with redshift, but the zeropoint does: that is high redshift ($z \simeq 2$) star-forming galaxies are forming stars at a higher rate than similar mass local galaxies. In Figure 8, we investigate this relation and star-formation histories for LBGs at $z \simeq$ 1.5–5. These quantities are based on best-fit SEDs, and their typical uncertainties are shown in the lower-right corner. The dotted lines are best-fit line obtained by keeping the logarithmic slope fixed at 0.90, estimated for star-forming galaxies at $z \leq 2$

(e.g., Elbaz et al. 2007; Daddi et al. 2007; Sawicki 2012). The dot-dash lines show the scatter from the best-fit line, which is ~0.6 dex for LBGs at $z \simeq 1$–3 and about 0.4 dex for LBGs at $z \simeq 4$–5. We also obtained the best-fit logarithmic slope for this relation, and found the fitted slope in the range of 0.81±0.30 for our LBG samples, which is consistent with 0.90 within the estimated 1σ scatter in this relation. We find that a proportionality with a logarithmic slope of 0.90 provides a good fit to the data with few outliers at stellar mass greater than 10^{10} $M_{\odot}$.

Finlator et al. (2006) have shown that tight relation exists between SFR and stellar mass for galaxies at $z \simeq 4$ using the cosmological hydrodynamic simulations, which is also consistent with the observations (Bouwens et al. 2011). Finlator et al. (2006) also point out that the scatter in the Figure 8 could be a measure of SFR 'burstiness' as a function of stellar mass. This means that the linear relation (with a logarithmic slope of ~0.90) indicate an average SFR for a given stellar mass, but galaxies can also experience bursts of up to two times the average SFR value at the same stellar mass as shown by the scatter. The scatter in the SFR versus stellar mass relation for LBGs at $z \simeq 1$–3 is slightly larger than ~0.3 dex — observed at $z \simeq 2$ by Daddi et al. (2007) — possibly because of few galaxies forming a sharp edge towards high SFR values, as shown in the relation for U_{225}- and U_{275}-dropouts (upper panel in Figure 8). These galaxies have low stellar ages (less than 10 Myr), which could be highly uncertain as discussed in § 3.3. It is also possible that this edge could be an artifact due to lower limits on the model parameters τ and t (e.g., Hainline et al. 2012). We also note that McLure et al. (2011) argue that the tightness in the SFR-stellar mass relation depends on the assumed SFH. The scatter in this relation is much less for a constant SFH, while it is much larger for other SFHs. Therefore, it is also likely that the larger scatter we see in Figure 8 could be due to different SFHs.

Figure 8 shows that, though our data has little more scatter compared to the MS relation at $z \lesssim 2$, the majority of our galaxies fall on to this relation characterized by a logarithmic slope of 0.90. A similar correlation is observed at $z \simeq 6$–8 by McLure et al. (2011), and supported by cosmological hydrodynamic simulations of Finlator et al. (2011). Our observations confirm this MS relation for star-forming galaxies from $z \simeq 1.5$ to 5, implying that — on average — their star-formation histories are similar.

4.3. Implications

In previous sections, we have shown that LBGs at $z \simeq 1$–3 — on average — are massive, dustier, and have higher star-formation rates than LBGs at $z \simeq 4$–5 with similar luminosities, though it should also be noted that they are not very different within estimated 1σ

uncertainties. As pointed out by Papovich et al. (2011), the number densities of galaxies at fixed luminosity could change substantially over this redshift range, which could lead to potential biases when comparing galaxies at different redshifts. However, the general trends we observe in stellar masses, SFRs, and dust extinction are supported by other independent means. The characteristics UV luminosity ($L^*_{\rm uv}$) is increasing as a function of redshift from $z \sim 8$ to 2 (e.g., H10), which implies increase in SFRs with time, while Finkelstein et al. (2010) have shown that stellar masses for $M^*_{\rm uv}$ LBGs grow from $z \simeq 8$ to 2. The UV spectral slope β shows evolution as a function of redshift (Figure 4), which could indicate lower dust content at higher redshifts. The higher dust content in LBGs at lower redshift is also in accordance with the studies at $z \simeq 1$ (e.g., Burgarella et al. 2007; Basu-Zych et al. 2011), while the Verma et al. (2007) supports the lower dust content in LBGs at $z \simeq 5$. Therefore, the ensemble properties of LBGs in our sample are in general agreement with the expected results.

The stellar mass–UV luminosity relation (Figure 7) and the SFR–stellar mass relation (Figure 8) are based on measurements from best-fit SEDs, therefore, it is possible that these quantities are not totally independent which might affect their observed correlations. To investigate this, we show distributions of mass-to-light (M/L; Mass/$L_{\rm uv}$) ratios and specific SFRs (SSFR; SFR/Mass) in Figure 9. The black (red) histograms show distribution for LBGs at $z \simeq 1$–3 ($z \simeq 4$–5), and the median values are shown by dashed vertical lines. The median values of M/L ratio and SSFR for LBGs at $z \simeq 4$–5 are slightly lower than that at $z \simeq 1$–3, but are still consistent within the 1σ uncertainties as shown by the error bar on the top of the black histogram. A two-sided K-S test indicates a probability *less* than 0.05 that the distributions (red and black histograms) are drawn from the *same* parent distribution. The constancy of the M/L ratio and SSFR between $z \simeq 1.5$ and 5 agrees very well with the constant slope we find in Figure 7 and Figure 8 for our sample of LBGs.

Stellar masses of LBGs at $z \simeq 1$–3 are generally well correlated with UV absolute magnitude and current SFR, as expected for star-forming galaxies at similar redshifts (e.g., Elbaz et al. 2007; Daddi et al. 2007; Sawicki 2012). These correlations implies very similar mass assembly and SFH for these galaxies, but the exact nature of SFHs is still not clearly understood. Papovich et al. (2011) showed that the cosmologically averaged SFRs of star-forming galaxies at $3 < z < 8$ — at constant co-moving number density — increase smoothly from $z = 8$ to 3, and the stellar mass growth in these galaxies is consistent with this derived SFH. The scenario of rising SFH (see also Lee et al. 2010) is also supported by recent results from the cosmological hydrodynamic simulations (e.g., Finlator et al. 2011). The models with rising SFHs conflicts with the assumptions that the SFR in distant galaxies is either constant or decreasing exponentially with time (e.g., Papovich et al. 2005; Shapley et al. 2005; Labbé et al. 2010). Though, we remind the reader that the models with rising SFHs advo-

cated by Papovich et al. (2011) and others correspond to a cosmologically averaged SFHs for typical galaxies, and not individual galaxies, because they could involve random events that changes their instantaneous SFR. Papovich et al. (2011) and Lee et al. (2010) also argue that rising SFHs are most beneficial to higher redshift ($z \gtrsim 3$) galaxies. We find that for our assumed SED model parameters, the LBGs between redshift $z \simeq 1.5$ and 5 — on average — have similar SFHs, though the precise nature of SFHs at all redshift is still under debate, and could also affect the SFR–stellar mass correlation.

Our analysis demonstrates that the dropout selected galaxies at $z \simeq 1$–3 — within luminosities probed here — show similar correlations between physical parameters (SFR, stellar mass, UV luminosity) as other star-forming galaxies selected using different color criteria (e.g., $sBzK$, BX/BM) at $z \simeq 2$. This is consistent with the Ly et al. (2011) conclusion that majority (~80–90%) of the dropout selected galaxies overlap with other color selected star-forming galaxies with stellar masses less than 10^{10} $M_\odot$. The stellar mass range for our current sample is between $\sim 10^8$ and $\sim 10^{10}$ $M_\odot$, with sample completeness around $10^{9--9.5}$ $M_\odot$. Significant differences between the dropout selected sample and other color selected samples of star-forming galaxies at $z \simeq 2$ exists for massive galaxies ($\gtrsim 10^{10}$ $M_\odot$; Ly et al. 2011). Therefore, it is vital to use uniform selection technique at all redshifts to avoid any selection biases. The Lyman break dropout technique is the most convenient and widely used method to select galaxies at $z \gtrsim 3$, and we have shown that LBGs at $z \simeq 1$–3 selected using this dropout technique have similar physical properties (within uncertainties) as LBGs at $z \simeq 4$–5 with similar luminosities. Hence, LBG selection at $z < 3$ is important to understand properties of LBGs and properly investigate their evolution as a function of redshift. The validity of LBG properties over wide luminosity and mass range can be investigated in detail with the upcoming and future WFC3 UV surveys such as CANDELS (Grogin et al. 2011; Koekemoer et al. 2011) and the WFC3 UV UDF (Rafelski et al. 2012, PI: H. Teplitz).

5. Summary

In this paper, we investigated stellar populations of LBGs at $z \simeq 1$–3 selected using *HST*/WFC3 UVIS filters in the GOODS-S field. We used deep multi-wavelength observations from the *HST*, VLT, and *Spitzer* to compare observed SEDs with the spectral synthesis models to infer physical properties (stellar masses, stellar ages, SFRs, and dust extinction) of these LBGs. We also compared these LBGs with their higher redshift ($z \simeq 4$–5) counterparts. Our results can be summarized as follows:

• We obtain reliable photometric redshifts for dropout selected LBGs at $z \simeq 1$–3 based on 10–13 band SEDs.

• The UV continuum slope β for LBGs at $z \simeq 1$–3 is redder compared to their higher redshift counterparts, implying higher dust content in these LBGs.

• On average, LBGs at $z \simeq 1$–3 are massive, dustier and more highly star-forming compared to LBGs at $z \simeq 4$–5, though their median values are very similar within estimated 1σ uncertainties. This similarity emphasizes the importance of identical Lyman break selection technique at all redshifts, which selects physically similar galaxies.

• The stellar mass–absolute UV magnitude relation for LBGs between $z \simeq 1.5$ and 5 show linear correlation with a logarithmic slope of $\sim$0.46, while the SFR–stellar mass relation show similar correlation with a logarithmic slope of $\sim$0.90. To properly compare and interpret such relations at higher ($z > 3$) redshift, and to avoid any selection biases due to different selection techniques, a true Lyman break selection is required at $z \simeq 2$.

• We need larger *HST* UV surveys to cover full range in luminosity/mass and better understand LBG properties, and their evolution. Both deeper and wider UV surveys are needed. The wider one to probe the high mass end, while the deeper one will probe the sub-L^* population. A large number of *HST* orbits have been used for dropout selected galaxies at $z > 3$, and the lower redshift regime needs to be explored in a comparable manner.

This paper is based on Early Release Science observations made by the WFC3 Scientific Oversight Committee. We are grateful to the Director of the Space Telescope Science Institute for awarding Director's Discretionary time for this program. Support for program #11359 was provided by NASA through a grant HST-GO-11359.08-A from the Space Telescope Science Institute, which is operated by the Association of Universities for Research in Astronomy, Inc., under NASA contract NAS 5-26555. This research was (partially) supported by a grant from the American Astronomical Society.

REFERENCES

Adelberger, K. L., Steidel, C. C., Shapley, A. E., et al. 2004, ApJ, 607, 226

Arnouts, S., Cristiani, S., Moscardini, L., et al. 1999, MNRAS, 310, 540

Atek, H., Siana, B., Scarlata, C., et al. 2011, ApJ, 743, 121

Balestra, I., Mainieri, V., Popesso, P., et al. 2010, A&A, 512, 12

Basu-Zych, A. R., Hornschemeier, A. E., Hoversten, E. A., Lehmer, B., & Gronwall, C. 2011, ApJ, 739, 98

Bertin, E., & Arnouts, S. 1996, A&AS, 117, 393

Bouwens, R. J., Illingworth, G. D., Blakeslee, J. P., & Franx, M. 2006, ApJ, 653, 53

Bouwens, R. J., Illingworth, G. D., Franx, M., & Ford, H. 2007, ApJ, 670, 928

Bouwens, R. J., Illingworth, G. D., Franx, M., et al. 2009, ApJ, 705, 936

Bouwens, R. J., Illingworth, G. D., Oesch, P. A., et al. 2010, ApJ, 709, L133

Bouwens, R. J., Illingworth, G. D., Oesch, P. A., et al. 2011, ApJ, in press (arXiv:1109.0994)

Bruzual, G., & Charlot, S. 2003, MNRAS, 344, 1000

Burgarella, D., Le Floćh, E., Takeuchi, T. T., et al. 2007, MNRAS, 380, 986

Calzetti, D., Kinney, A. L., & Storchi-Bergmann, T. 1994, ApJ, 429, 582

Calzetti, D., Armus, L., Bohlin, R. C., et al. 2000, ApJ, 533, 682

Cooper, M. C., Yan, R., Dickinson, M., et al. 2011, MNRAS, submitted (arXiv:1112.0312)

Daddi, E., Cimatti, A., Renzini, A., et al. 2004, ApJ, 617, 746

Daddi, E., Dickinson, M., Morrison, G., et al. 2007, ApJ, 670, 156

Dahlen, T., Mobasher, B., Dickinson, M., et al. 2010, ApJ, 724, 425

Elbaz, D., Daddi, E., Le Borgne, D., et al. 2007, A&A, 468, 33

Erb, D. K., Shapley, A. E., Pettini, M., et al. 2006, ApJ, 644, 813

Finkelstein, S. L., Papovich, C., Giavalisco, M., et al. 2010, ApJ, 719, 1250

Finkelstein, S. L., Hill, G. J., Gebhardt, K., et al. 2011, ApJ, 729, 140

Finkelstein, S. L., Papovich, C., Salmon, B., et al. 2012, ApJ, submitted (arXiv:1110.3785)

Finlator, K., Davé, R., Papovich, C., & Hernquist, L. 2006, ApJ, 639, 672

Finlator, K., Davé, R. & Oppenheimer, B. D. 2007, MNRAS, 376, 1861

Finlator, K., Oppenheimer, B. D., & Davé, R. 2011, MNRAS, 410, 1703

Giavalisco, M., Ferguson, H. C., Koekemoer, A. M., et al. 2004, ApJ, 600, L93

Grazian, A.,Fontana, A., de Santis, C., et al. 2006, A&A, 449, 951

Grogin, N.A., Kocevski, D. D., Faber, S. M., et al. 2011, ApJS, 197, 35

Guhathakurta, P., Tyson, J. A., & Majewski, S. R. 1990, ApJ, 357, L9

Haberzettl, L., Williger, G., Lehnert, M. D., Nesvadba, N., & Davies, L. 2012, ApJ, 745, 96

Hainline, K. N., Shapley, A. E., Greene, J. E., et al. 2012, ApJ, submitted (arXiv:1206.3308)

Hathi, N. P., Malhotra, S., & Rhoads, J. 2008a, ApJ, 673, 686

Hathi, N. P., Jansen, R. A., Windhorst, R. A., et al. 2008b, AJ, 135, 156

Hathi, N. P., Ryan, R. E., Cohen, S. H., et al. 2010, ApJ, 720, 1708 (H10)

Ilbert, O., Arnouts, S., McCracken, H. J., et al. 2006, A&A, 457, 841

Ilbert, O., Capak, P., Salvato, M., et al. 2009, ApJ, 690, 1236

Kennicutt, R. C., Jr. 1998, ARA&A, 36, 189

Koekemoer, A. M., Faber, S. M., Ferguson, H. C., et al. 2011, ApJS, 197, 36

Komatsu, E., Dunkley, J., Nolta, M. R., et al. 2009, ApJS, 180, 330

Labbé, I., González, V., Bouwens, R. J., et al. 2010, ApJ, 708, L26

Lee, S.-K., Ferguson, H. C., Somerville, R. S., Wiklind, T., & Giavalisco, M. 2010, ApJ, 725, 1644

Leitherer, C., Schaerer, D., Goldader, J. D., et al. 1999, ApJS, 123, 3

Ly, C., Malkan, M. A., Treu, T., et al. 2009, ApJ, 697, 1410

Ly, C., Malkan, M. A., Hayashi, M., et al. 2011, ApJ, 735, 91

Madau, P. 1995, ApJ, 441, 18

McLure, R. J., Dunlop, J. S., de Ravel, L., et al. 2011, MNRAS, 418, 2074

Noeske, K. G., Weiner, B. J., Faber, S. M., et al. 2007, ApJ, 660, L43

Oesch, P. A., Bouwens, R. J., Carollo, C. M., et al. 2010, ApJ, 725, L150

Oke, J. B., & Gunn, J. E. 1983, ApJ, 266, 713

Papovich, C., Dickinson, M., & Ferguson, H. C. 2001, ApJ, 559, 620

Papovich, C., Dickinson, M., Giavalisco, M., Conselice, C., & Ferguson, H. C. 2005, ApJ, 631, 101

Papovich, C., Finkelstein, S. L., Ferguson, H. C., Lotz, J. M., & Giavalisco, M. 2011, MNRAS, 412, 1123

Rafelski, M., Teplitz, H., Grogin, N., et al. 2012, AAS 220, 421.04

Ravikumar, C. D., Puech, M., Flores, H., et al. 2007, A&A, 465, 1099

Reddy, N. A., & Steidel, C. C. 2009, ApJ, 692, 778

Santini, P., Fontana, A., Grazian, A., et al. 2009, A&A, 504, 751

Sawicki, M. 2012, MNRAS, 421, 2187

Schaerer, D., & de Barros, S. 2009, A&A, 502, 423

Shapley, A. E., Steidel, C. C., Erb, D. K., et al. 2005, ApJ, 626, 698

Stanway, E. R., McMahon, R. G., & Bunker, A. J. 2005, MNRAS, 359, 1184

Stark, D. P., Ellis, R. S., Bunker, A., et al. 2009, ApJ, 697, 1493

Stark, D. P., Ellis, R. S., Chiu, K., Ouchi, M., & Bunker, A. 2010, MNRAS, 408, 1628

Steidel, C. C., Giavalisco, M., Pettini, M., Dickinson, M., & Adelberger, K. L. 1996, ApJ, 462, L17

Steidel, C. C., Adelberger, K. L., Giavalisco, M., Dickinson, M., & Pettini, M. 1999, ApJ, 519, 1

Steidel, C. C., Shapley, A. E., Pettini, M., et al. 2004, ApJ, 604, 534

Vanzella, E., Cristiani, S., Dickinson, M., et al. 2008, A&A, 478, 83

Verma, A., Lehnert, M. D., Förster Schreiber, N. M., Bremer, M. N., & Douglas, L. 2007, MNRAS, 377, 1024

Wilkins, S. M., Bunker, A. J., Stanway, E., Lorenzoni, S., & Caruana, J. 2011, MNRAS, 417, 717

Windhorst, R. A., Cohen, S. H., Hathi, N. P., et al. 2011, ApJS, 193, 27

Wuyts, S., Labbé, I., Förster Schreiber, N. M., et al. 2008, ApJ, 682, 985

Xue, Y. Q., Luo, B., Brandt, W. N., et al. 2011, ApJS, 195, 10

Yan, H., Windhorst, R. A., Hathi, N. P., et al. 2010, RA&A, 10, 867

This preprint was prepared with the AAS LaTeX macros v5.2.

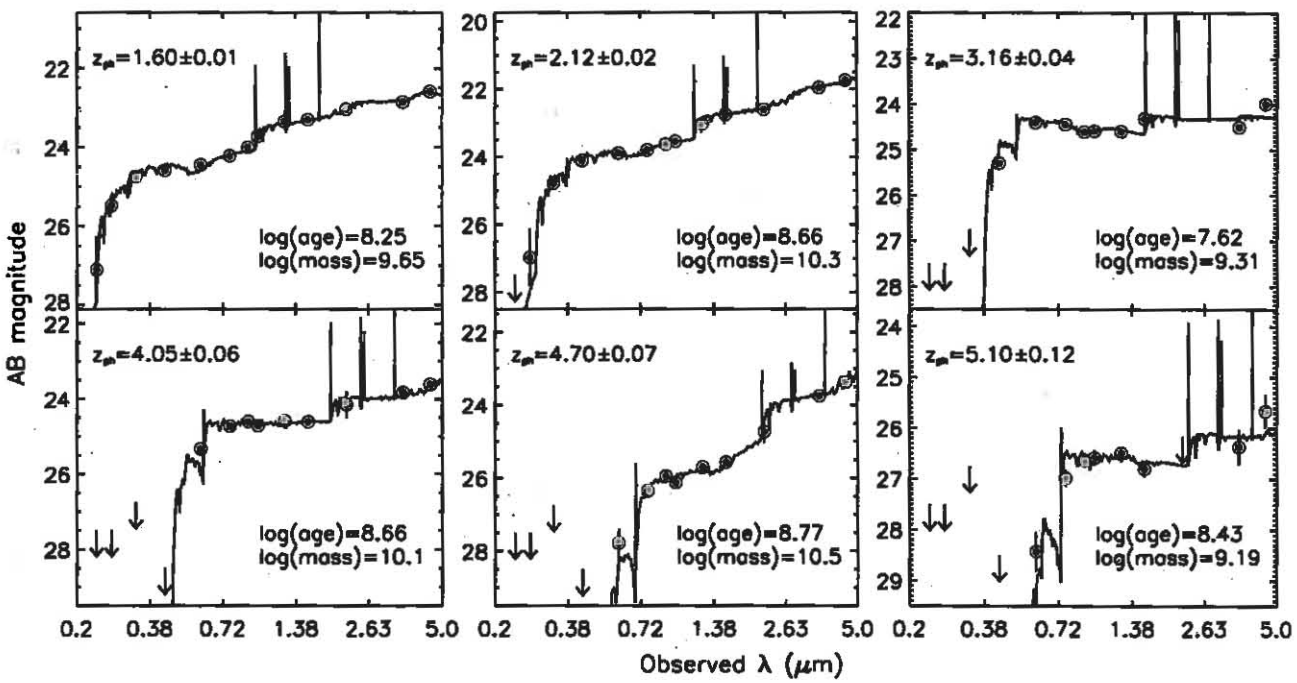

Fig. 1.— [Top panel] Example best-fit SEDs of LBGs at $z \simeq 1$–3. We have used the Le PHARE code (Arnouts et al. 1999; Ilbert et al. 2006) to compute photometric redshifts and to perform SED fitting. Grey concentric circles are observed magnitudes in three *HST*/WFC3 UVIS, four *HST*/ACS, three *HST*/WFC3 IR, one VLT Ks, and two *Spitzer*/IRAC [3.6], [4.5] bands. [Bottom panel] Same as the top panel but for the comparison sample of LBGs at $z \simeq 4$–5. Stellar masses are in solar units and stellar ages are in years.

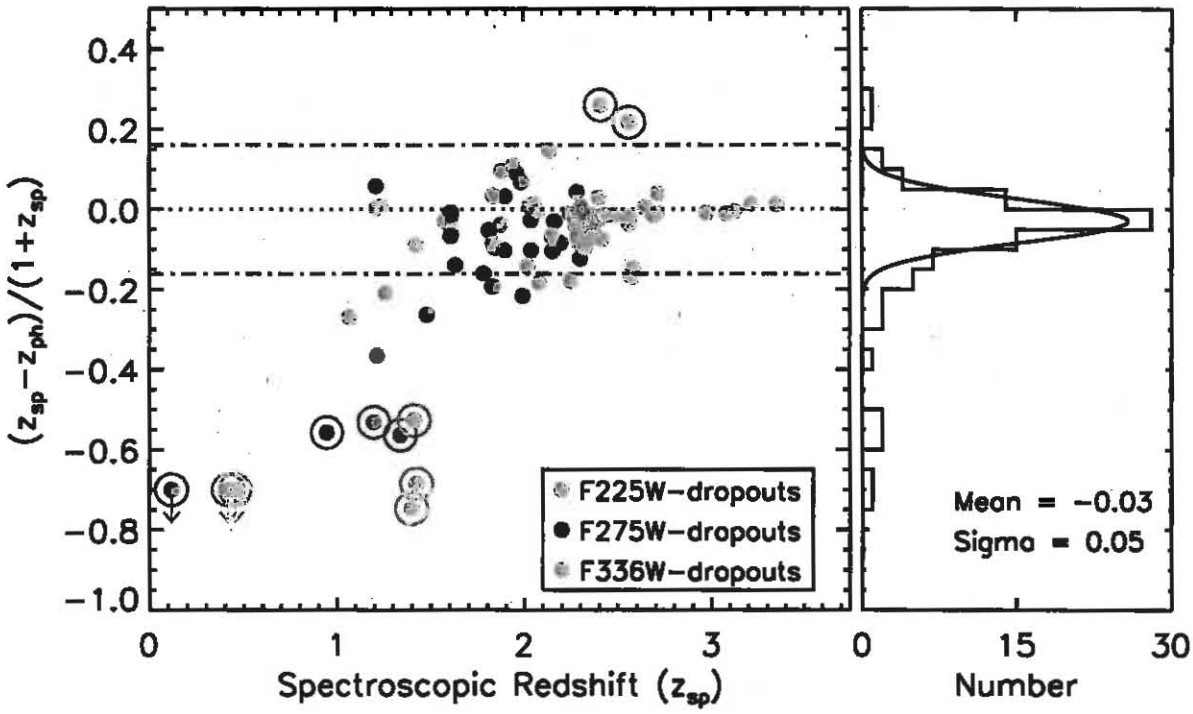

Fig. 2.— Comparison of the SED-based photometric redshifts with the publicly available spectroscopic redshifts for LBGs at $z \simeq 1$–3. The concentric circles indicate unreliable spectroscopic redshifts based on their quality flags. The dotted line shows the 1-to-1 relation between two redshifts. The histogram shows distribution of $(z_{sp} - z_{ph}/1{+}z_{sp})$, and the 1σ uncertainties in this distribution is ~5%. The dot-dash lines show 3σ limits.

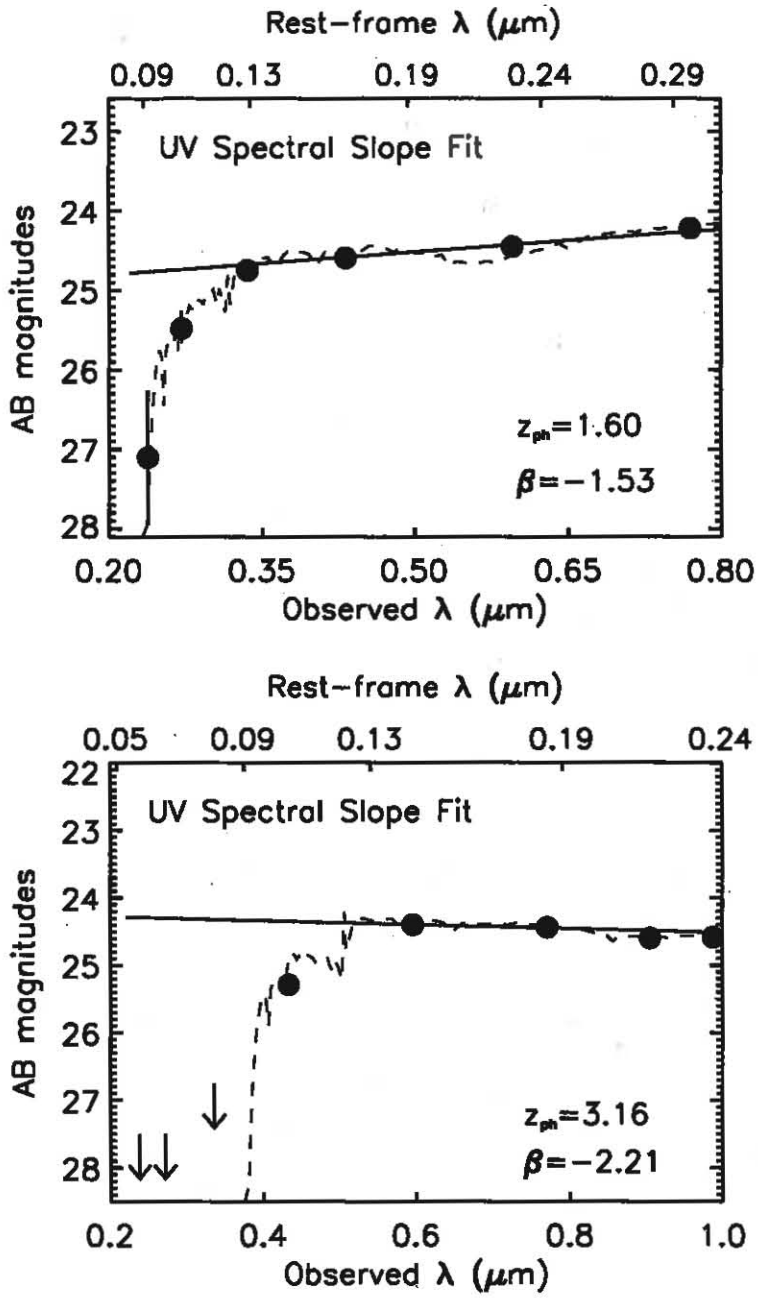

Fig. 3.— Example fitting of the UV spectral slope β to best-fit SEDs for two LBGs from the $z \simeq 1$–3 sample. The dotted black line is the best-fit SED, while solid black line shows the estimated UV continuum slope β. The black filled circles are observed magnitudes. We test two different rest-frame UV wavelength range (1300–1900 Å and 1300–3400 Å) to address the robustness of our estimated UV continuum slope β, and find similar median slopes within 1σ scatter.

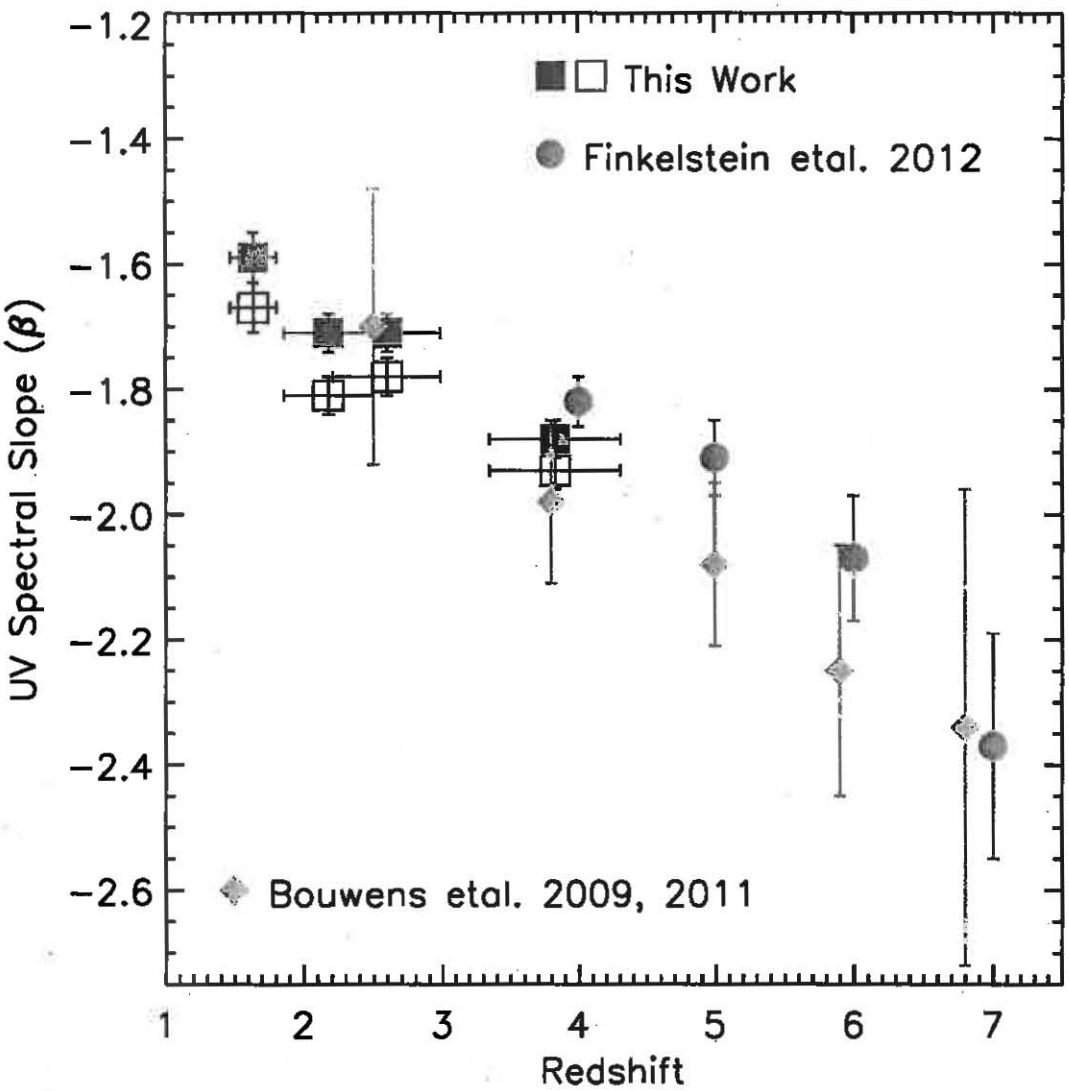

Fig. 4.— UV spectral slope β as a function of redshift. Blue filled squares indicate the median β values when we fit rest-frame 1300 to 1900 Å wavelengths, and blue open squares indicate βs when we fit 1300 to 3400 Å. The higher redshift ($z \gtrsim 2.5$) measurements from Finkelstein et al. (2012) and Bouwens et al. (2009, 2011) are also shown for comparison. Ours and the Finkelstein et al. (2012) uncertainties are the standard error of the mean, while uncertainties from Bouwens et al. are 1σ scatter. For comparison, our 1σ uncertainties are listed in Table 1.

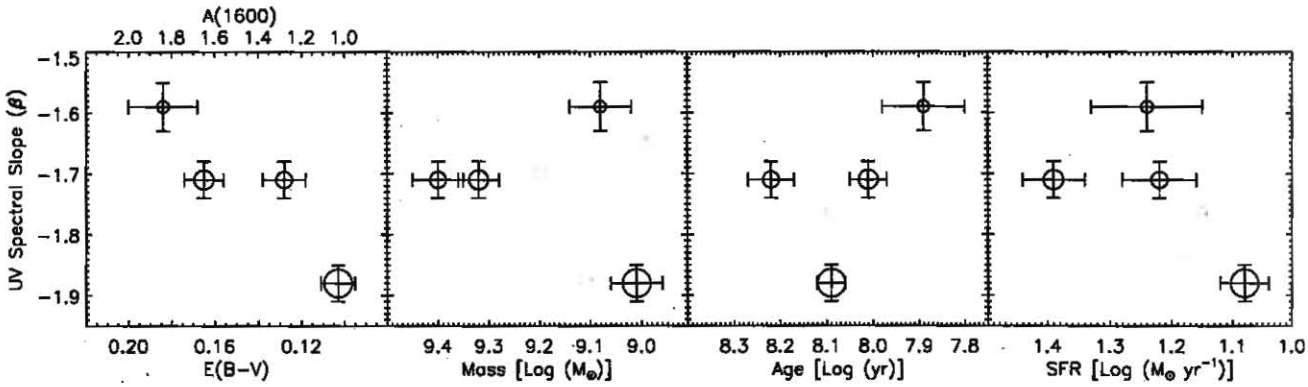

Fig. 5.— UV spectral slope β versus best-fit SED parameters (E(B-V), stellar mass, stellar age, star-formation rate). The size of the circle increases with redshift i.e., the smallest circle correspond to the lowest redshift bin ($z \simeq 1.6$), and the largest circle correspond to $z \simeq 4$–5 bin. The changes in the UV-continuum slope β from $z \simeq 1.6$ to 5 are most likely due to the change (factor of $\sim$2 or 0.3 dex) in the dust content E(B–V) of the galaxies, as other parameters show smaller variation as a function of redshift.

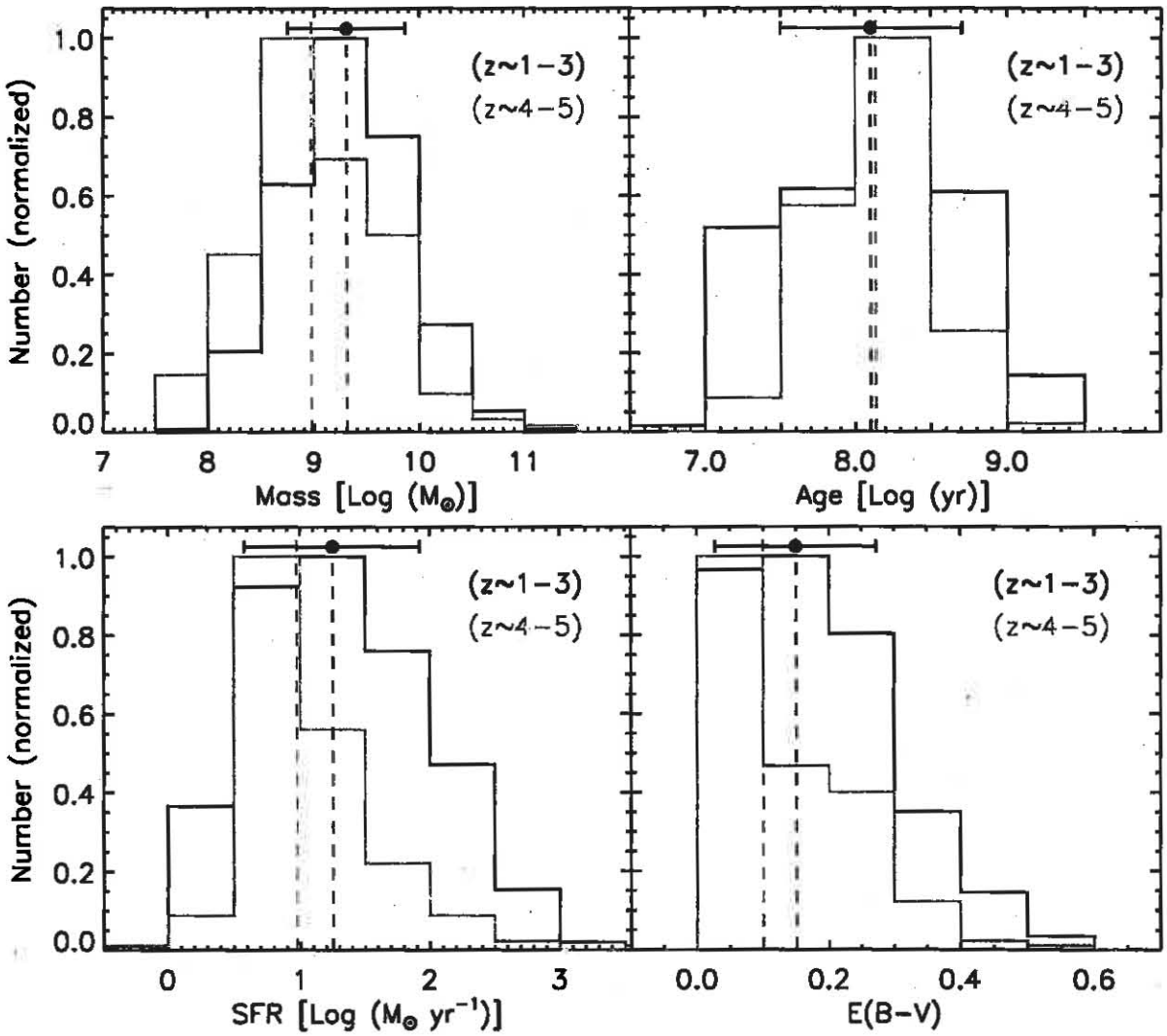

Fig. 6.— Distribution of stellar masses, stellar ages, star-formation rates, and dust extinction for LBGs at $z \simeq 1$–3 (black) and the comparison sample at $z \simeq 4$–5 (red). All four parameters are estimated from the best-fit SEDs. Median values are shown by vertical dashed lines and 1σ uncertainties are shown by an error bar at the top of the black histogram. Though the higher redshift LBGs have, on average, lower values of most of these physical parameters than LBGs at $z \simeq 1$–3, the median values are similar within estimated uncertainties. Stellar ages do not show any clear evolution with redshift mainly because of higher uncertainties in their measurements (see § 3.3). The histograms show normalized numbers for both samples (total number of galaxies in each sample is shown in Table 1), and a two-sided K-S test indicates a probability $P \lesssim 0.006$ that the two distributions are drawn from the same parent distribution.

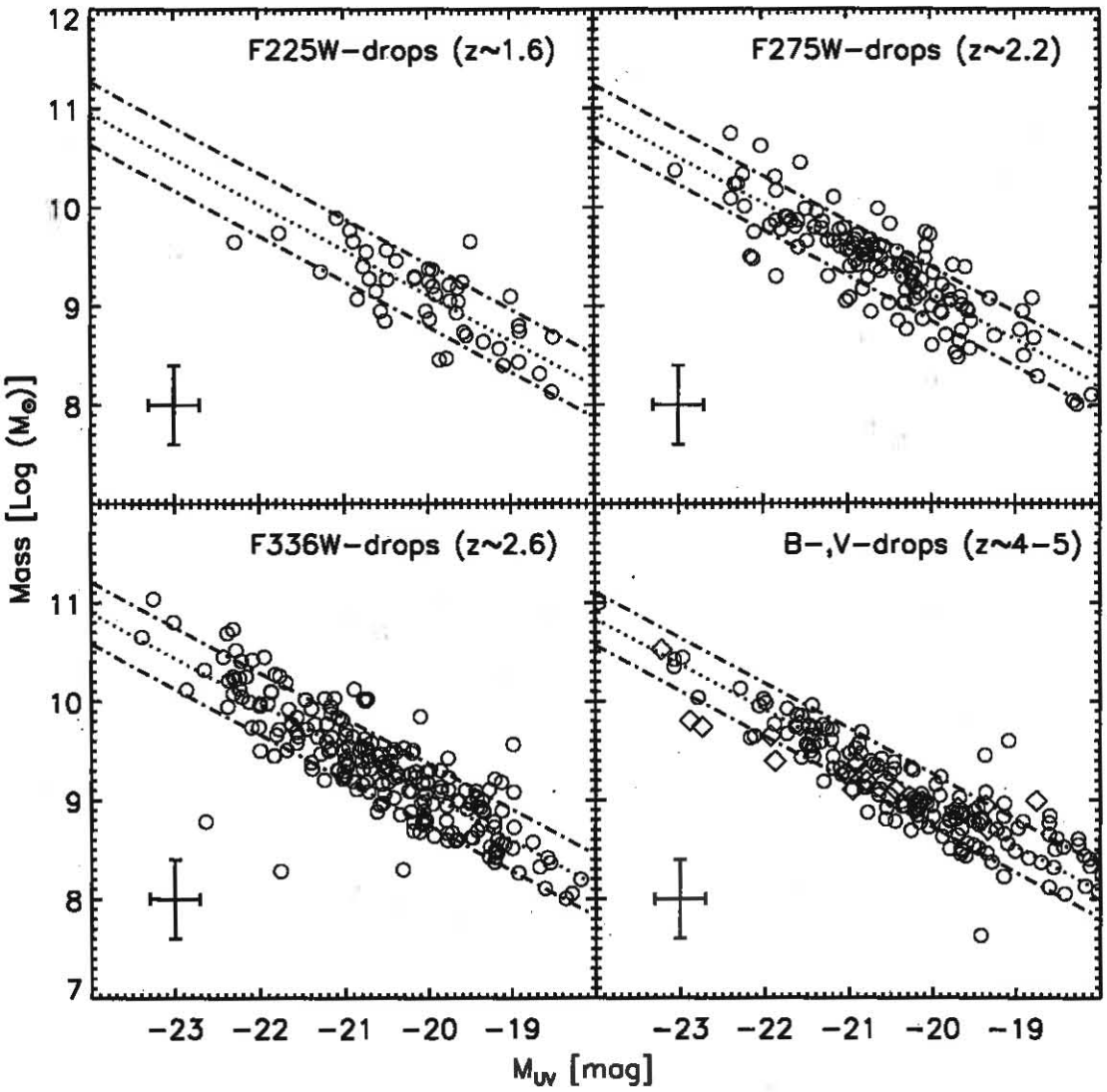

Fig. 7.— Stellar mass versus UV absolute magnitude relation for U_{225}-, U_{275}-, U_{336}-dropout samples. Bottom right panel shows the same relation for the comparison sample of LBGs at $z \simeq 4$–5 (black circles for $z \simeq 4$, and black squares for $z \simeq 5$). The average uncertainties are shown in the bottom-left corner. The dotted black line is the best-fit line with a logarithmic slope of 0.46. The dot-dash line shows the 1σ scatter ($\sim$0.3 dex) from the best-fit linear relation.

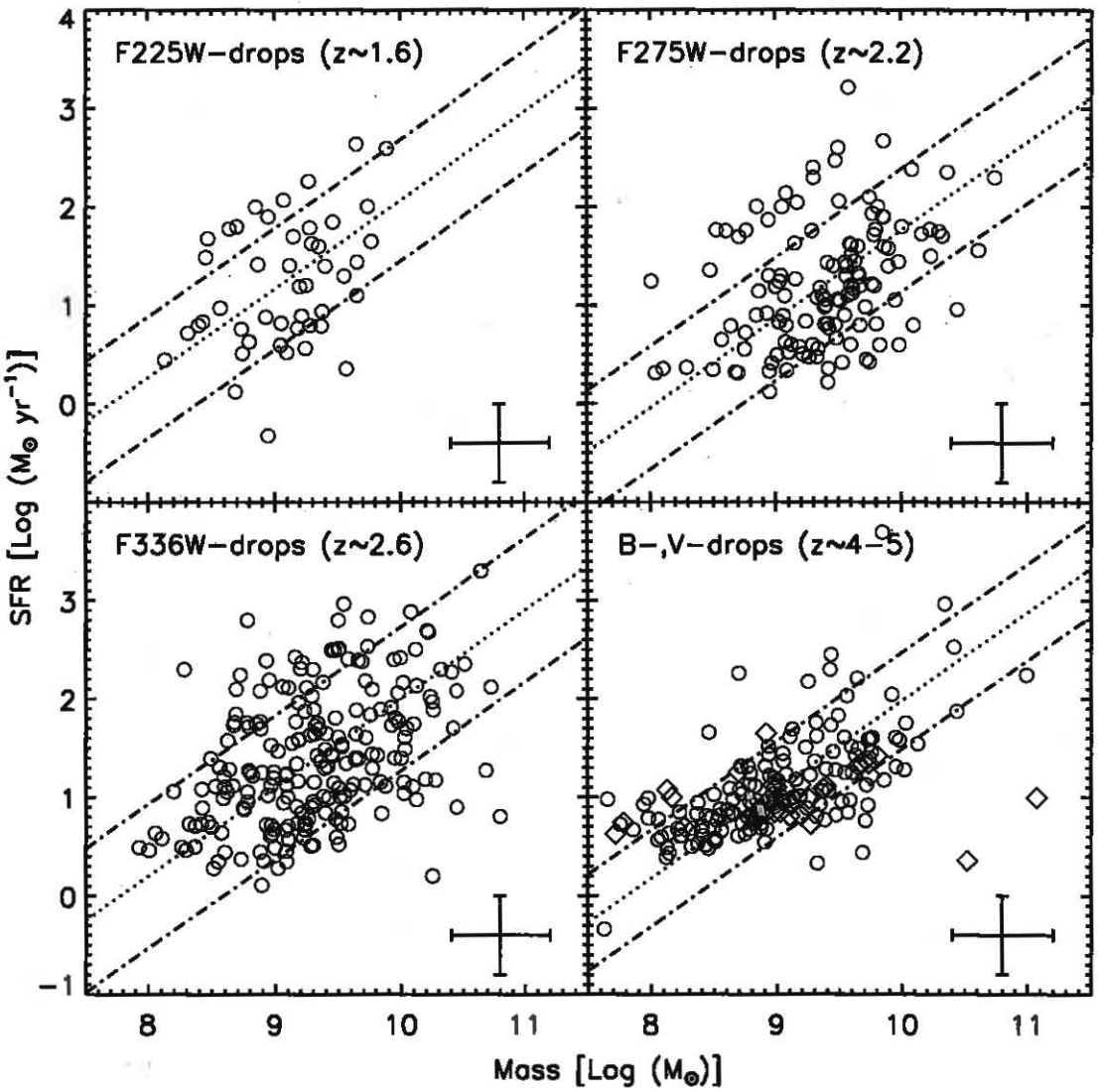

Fig. 8.— Stellar mass versus SFR relation for U_{225}-, U_{275}-, U_{336}-dropout samples. Bottom right panel shows the same relation for the comparison sample of LBGs at $z \simeq 4$–5 (black circles for $z \simeq 4$, and black squares for $z \simeq 5$). The average uncertainties are shown in the bottom-right corner. The dotted black line is the best-fit line with a logarithmic slope of 0.90. The dot-dash line shows the 1σ scatter ($\sim$0.6 dex, $\sim$0.4 dex for $z \simeq 4$–5) from the best-fit linear relation. In the upper panel, few galaxies form a sharp edge towards high SFR values, which could be an artifact due to lower limits on the model parameters τ and t (e.g., Hainline et al. 2012).

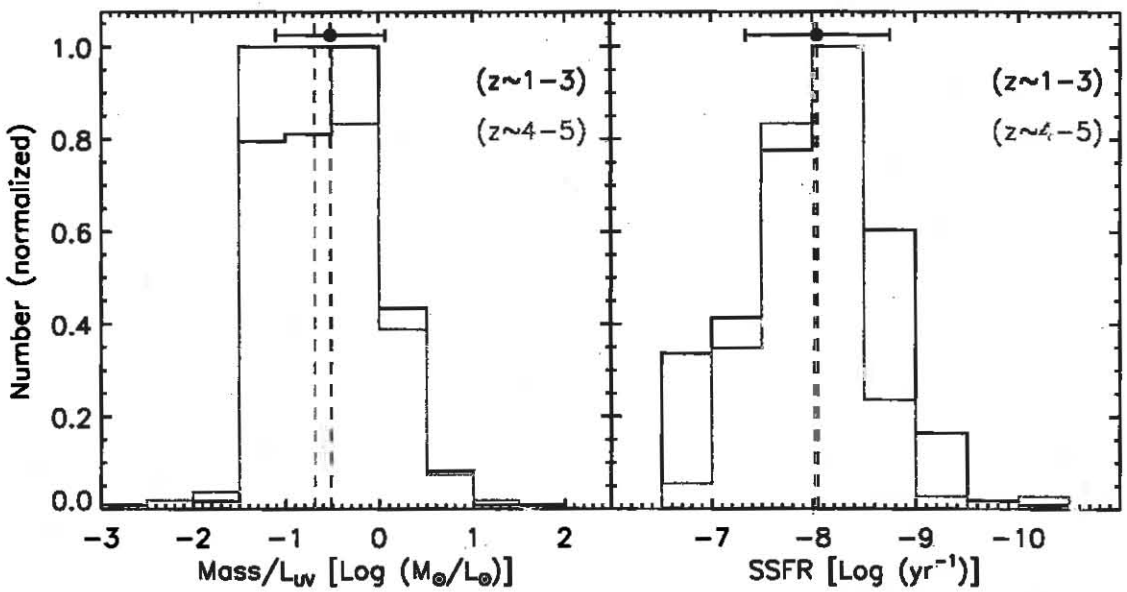

Fig. 9.— Distribution of mass-to-light ratios and specific SFRs for LBGs at $z \simeq 1$–3 (black) and for the comparison sample at $z \simeq 4$–5 (red). Median values are shown by vertical dashed lines and 1σ uncertainties are shown by an error bar at the top of the black histogram. Though the higher redshift LBGs have, on average, lower values of these parameters than LBGs at $z \simeq 1$–3, the median values are similar within estimated uncertainties. The histograms show normalized numbers for both samples (total number of galaxies in each sample is shown in Table 1), and a two-sided K-S test indicates a probability $P \lesssim 0.05$ that the two distributions are drawn from the same parent distribution.

Table 1. UV Spectral Slopes (β)

Redshift $< z >$	Number of Galaxies (N)	UV Slope[a] β	1σ scatter	SEM[b]
1.6 (±0.2)	47	−1.59 (−1.67)	0.29 (0.27)	0.04 (0.04)
2.2 (±0.3)	126	−1.71 (−1.81)	0.34 (0.37)	0.03 (0.03)
2.6 (±0.4)	213	−1.71 (−1.78)	0.47 (0.50)	0.03 (0.03)
3.8[c] (±0.5)	182	−1.88 (−1.93)	0.45 (0.41)	0.03 (0.03)

[a]The UV continuum slope β is estimated from best-fit SEDs by fitting a line between the rest-frame wavelengths 1300–1900 Å (1300–3400 Å)

[b]The standard error of the mean = (1σ scatter)/$\sqrt{N}$

[c]The comparison sample of B_{435}- and V_{606}-dropouts. Because of small number of V_{606}-dropouts, the average/median redshift is similar to a B_{435}-dropout.